ACS APPLIED MATERIALS & INTERFACES

Research Article

www.acsami.org

Hydrophilic, Bactericidal Nanoheater-Enabled Reverse Osmosis Membranes to Improve Fouling Resistance

Jessica R. Ray,[†] Sirimuvva Tadepalli,[‡] Saide Z. Nergiz,[‡] Keng-Ku Liu,[‡] Le You,[†] Yinjie Tang,[†] Srikanth Singamaneni,*[,‡] and Young-Shin Jun*[,†]

[†]Department of Energy, Environmental & Chemical Engineering, Washington University in St. Louis, 1 Brookings Drive, St. Louis, Missouri 63130, United States

[‡]Department of Mechanical Engineering & Materials Science, Institute of Materials Science & Engineering, Washington University in St. Louis, 1 Brookings Drive, St. Louis, Missouri 63130, United States

Supporting Information

ABSTRACT: Polyamide (PA) semipermeable membranes typically used for reverse osmosis water treatment processes are prone to fouling, which reduces the amount and quality of water produced. By synergistically coupling the photothermal and bactericidal properties of graphene oxide (GO) nanosheets, gold nanostars (AuNS), and hydrophilic polyethylene glycol (PEG) on PA reverse osmosis membrane surfaces, we have dramatically improved fouling resistance of these membranes. Batch fouling experiments from three classes of fouling are presented: mineral scaling ($CaCO_3$ and $CaSO_4$), organic fouling (humic acid), and biofouling (*Escherichia coli*). Systematic analyses and a variety of complementary techniques were used to elucidate fouling resistance mechanisms from each layer of modification on the membrane surface. Both mineral scaling and organic fouling were significantly reduced in PA−GO−AuNS−PEG membranes compared to other membranes. The PA−GO−AuNS−PEG membrane was also effective in killing all near-surface bacteria compared to PA membranes. In the PA−GO−AuNS−PEG membrane, the GO nanosheets act as templates for *in situ* AuNS growth, which then facilitated localized heating upon irradiation by an 808 nm laser inactivating bacteria on the membrane surface. Furthermore, AuNS in the membrane assisted PEG in preventing mineral scaling on the membrane surface. In flow-through flux and foulant rejection tests, PA−GO−AuNS−PEG membranes performed better than PA membranes in the presence of $CaSO_4$ and humic acid model foulants. Therefore, the newly suggested membrane surface modifications will not only reduce fouling from RO feeds, but can improve overall membrane performance. Our innovative membrane design reported in this study can significantly extend the lifetime and water treatment efficacy of reverse osmosis membranes to alleviate escalating global water shortage from rising energy demands.

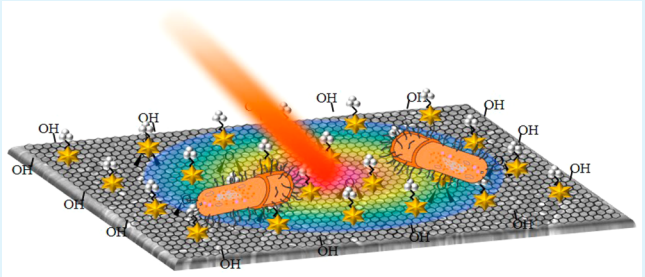

KEYWORDS: *reverse osmosis membranes, graphene oxide, gold nanostars, mineral scaling, organic fouling, biofouling*

1. INTRODUCTION

Reverse osmosis (RO) is a promising solution to supply drinking water for growing populations and relieve stress from rising water demands. In this high pressure process, brackish feed water is pumped across a semipermeable membrane, rejecting dissolved solutes and producing purified water.[1] Aromatic, polyamide thin film composite (TFC) membranes are commonly used as they are stable over a wide pH range (3−11), and are more chemically and physically stable than previous membranes.[2,3] However, they are also prone to fouling,[4,5] or the accumulation of undesirable materials on the membrane surface, which reduces drinking water quality and quantity.[6]

Three major fouling classes must be minimized during water treatment: mineral scaling, organic fouling, and biofouling.[7] Mineral scaling results when salt crystal precipitation cakes the membrane surface obstructing water flow.[8] Calcium carbonate ($CaCO_3$) and calcium sulfate ($CaSO_4$) are the most common mineral scalants due to typically high concentrations of Ca^{2+}, HCO_3^-, and SO_4^{2-} ions in brackish feed solutions,[9] and, thus, represented mineral scalants in this study. Humic acid, used to test organic fouling in this work,[10] also constitutes a large fraction of dissolved organic matter ubiquitous in natural waters[11] and wastewaters,[12] and has been demonstrated to significantly reduce water flux during RO processes.[10] In addition, microbial fouling or biofouling generally occurs when aqueous microbes grow at the membrane surface to form a biofilm layer.[13,14] Thus, biofouling is considered to be the main challenge of seawater RO affecting 70% of these processes.[15]

Received: December 29, 2014
Accepted: May 5, 2015
Published: May 5, 2015

DOI: 10.1021/am509174j
ACS Appl. Mater. Interfaces 2015, 7, 11117−11126

Therefore, this work employed *Escherichia coli* to model biofouling during RO processes.[16]

With the operational costs of extending membrane life by external means being considerable (e.g., adjusting pH, antiscalants, etc.),[8,17,18] it could be beneficial to modify the membrane surface itself to resist fouling. Numerous researchers have investigated the integration of nanomaterials, polymers, and other materials to engineer fouling-resistant membrane surfaces.[17,19,20] For example, Rahaman et al. modified the surface with hydrophilic, antifouling polymer layers and Ag nanoparticles to reduce bacterial and inorganic fouling.[21] Graphene oxide nanosheets possess inherent antibacterial properties as demonstrated by Akhavan et al. against *E. coli*[22] which has been used toward improving RO membranes.[23−25] While these functional membranes can reduce biofilm growth, inactivation of bacteria in these cases requires additional thermal or chemical treatment.

Photothermal treatment by nanomaterials can offer a unique solution, bypassing thermal or chemical treatments while achieving bacterial lysis. So far, Au nanoparticles have been extensively studied in medical applications to kill cancer cells,[26−29] owing to their localized surface plasmon resonance (LSPR) and consequential photothermal properties. In the photothermal effect, a fraction of incident light on a material is converted into thermal energy which induces local heating and cell damage by irradiating the region of interest with a light source. The easy ability to tune the absorption maximum of shape-controlled Au nanostructures compared to those of other materials (e.g., organic dyes, carbon nanotubes, or graphene flakes) makes them an attractive platform for photothermal applications. Furthermore, owing to localized surface plasmons, the optical cross-section of Au nanostructures is nearly 4−5 orders of magnitude higher than that of conventional organic dyes.[30]

Localized surface plasmon resonance involves the collective oscillation of dielectrically confined conduction electrons in metal or highly doped semiconducting nanoparticles.[31] At the LSPR wavelength, metal nanostructures exhibit large absorption and scattering cross sections of light.[32] The energy radiated as the plasmon oscillations decay forms the source of light scattered from the metal nanostructures. At the same time, oscillating electrons undergo collisions with other electrons, exciting intraband and interband transitions in the metal. Collisions with the lattice phonons, the surface of the nanostructures, and surface ligands further contribute to damping and dephasing of the surface plasmon. These nonradiative processes generate heat and correspond to the light absorption of the nanoparticles.[33] Photoexcitation of the metal nanostructures results in heated electron gas that cools rapidly by exchanging energy with the nanoparticle lattice, which in turn exchanges energy with the surrounding environment.[34,35]

Typically in photothermal studies of Au nanoparticles, cell treatment is conducted in bulk solution (i.e., *in vivo* or *in vitro*). Recently, there have been a few examples demonstrating photothermal destruction of multidrug resistant bacteria in suspended solution using plasmonic nanostructures as heating elements.[36] On the basis of these promising photothermal properties and applications of plasmonic nanostructures, we suggest utilizing Au nanostars (AuNS) to kill bacteria in feed solutions during the RO process. Applications of Au nanoparticles as plasmonic nanoheaters in RO membrane applications remain unexplored, and to our knowledge, there is no work utilizing light-mediated Au nanoparticle bacterial inactivation on RO membranes for improved biofouling resistance in water treatment applications. Moreover, the efficacy of Au nanoparticle photothermal treatment for inhibiting growth of overlying microbial films on membranes is not yet understood.

In this work, we have created a novel, four-layer RO membrane by functionalizing a commercial polyamide (PA) RO membrane with graphene oxide (GO), Au nanostars (AuNS), and polyethylene glycol (PEG) to synergistically improve PA membrane fouling resistance to mineral scalants ($CaCO_3$ and $CaSO_4$), organic matter (humic acid), and bacteria (*Escherichia coli*). While there have been previous studies investigating GO-modified[37−39] and PEG-modified[40−42] RO membrane surface modifications, the efficacies of these surface modifications were tested against only one or two types of foulants and often require additional treatments, particularly when bacterial inactivation is desired. The AuNS modification proposed in this work eliminates the need for additional treatment, and as demonstrated here, the resulting membrane can reduce fouling from all three major fouling classes. A suite of interdisciplinary and complementary surface and solution analytical techniques was used to elucidate fouling mechanisms on each of the membrane layer surfaces. For the first time, utilizing photothermally active nanoheaters, we demonstrated the ability to kill bacteria on RO membrane surfaces for improved biofouling resistance while the same membrane can reduce inorganic and organic fouling. The results from these experiments can offer new solutions in regenerative RO membranes for potential use in water treatment.

2. MATERIALS AND METHODS

2.1. Chemicals and Materials. All chemicals used were ACS grade. Commercially available BW30 reverse osmosis TFC membranes were purchased form Dow Filmtec (Vandalia, IL). Sodium bicarbonate ($NaHCO_3$, JT Baker, NJ), sodium sulfate (anhydrous, Na_2SO_4, Alfa Aesar, MA), and calcium chloride dihydrite ($CaCl_2.2H_2O$, EMD Chemicals, NJ) were used to generate the calcium salts. Humic acid from Sigma-Aldrich (St. Louis, MO) was used for the organic fouling experiments. Polyethylene glycol (PEG, Sigma-Aldrich, MO), ethylene glycol dimethacrylate (EGDMA, Sigma-Aldrich, MO), potassium persulfate (PP, Sigma-Aldrich, MO), and potassium disulfite (PD, Sigma-Aldrich, MO) were all purchased for the PEG hydrophilic surface modification. GO powder was purchased from Cheap Tubes, Inc. (Cambridgeport, VT). The 1-ethyl-3-(3-(dimethylamino)propyl carbodiimide) (EDC) and n-hydroxy succinimide (NHS) were purchased from ThermoScientific; MES monohydrate (BioXtra), Au(III) chloride trihydrate, and 0.9% sodium chloride solution (Sterile filtered) were purchased from Sigma-Aldrich. HEPES buffer 1 M solution (pH 7.3) was purchased from Fisher bioreagents.

2.2. Multifunctional Membrane Fabrication. *PA−PEG Membrane.* PA−PEG membranes served as control membrane substrates as commonly modified PA substrates which have been used in previous studies.[18,43] First, a PEG monomer solution was mixed with an EGDMA cross-linker solution to promote PEG polymerization. This mixture was stirred gently for approximately 5 min. Next, an equimolar PP and PD initiator solution was made which helps form radicals on the polyamide surface to which PEG can graft.[44] The initiator solution was mixed with the PEG and EGDMA solution to make the final reaction solution. The final concentrations of PEG, EGMDA, PP, and PD were 0.1, 0.01, and 0.025 M, respectively.

PA−GO Membrane. To modify the membranes with GO, we used a previously reported approach with modifications.[45] Briefly, TFC membranes were exposed to a solution of 4 mM EDC, 10 mM NHS, and 0.5 M NaCl in 10 mM MES buffer at pH 5 for 1 h to convert the native carboxyl groups of the PA layer into amine reactive esters. The

DOI: 10.1021/am509174j
ACS Appl. Mater. Interfaces 2015, 7, 11117−11126

membrane was washed with ultrapure deionized (DI) water (resistivity >18.2 MΩ cm) and contacted with a solution of 10 mM ethylene diamine (ED), 0.15 mM NaCl in 10 mM HEPES buffer, at pH 7.5 to form amide bonds with activated esters. The membranes were washed to remove unlinked ED. GO powder was dissolved in 10 mM MES monohydrate buffer at pH 6 to form a 1 mg/mL solution. A mixture of 2 mM of EDC and 5 mM NHS was added to the 0.25 mg/mL GO solution in MES buffer to again convert the carboxyl groups on GO to amine reactive esters. This pH was adjusted to 7.2 before contacting the GO solution with membranes. The GO suspension was brought in contact with the membranes under constant agitation for 15 min. The membranes were then rinsed with ultrapure DI water and sonicated for 2 min to remove unbound GO. The membranes were stored at 4 °C until use.

PA−GO−AuNS−PEG Membrane. GO-modified membranes (PA−GO) were used for *in situ* growth of Au nanostars (AuNS). The membranes were brought in contact with a solution of 10 mL of 100 mM HEPES immediately after adding 40 μL of aqueous $HAuCl_4$ solution. The membranes were placed vertically to avoid nonspecific adsorption and accumulation of AuNS precipitated from solution. After *in situ* growth for 3 h, the membranes were washed thoroughly to remove any loosely bound AuNS. Our previous work demonstrated the growth of AuNS on GO nanosheets in solution.[29] However, in the case of AuNS on membrane surfaces, it is difficult to measure the optical properties of GO-templated *in situ* AuNS growth on TFC membranes because the membrane surface is rough and opaque. Therefore, a glass substrate was modified with GO then used to grow AuNS *in situ* to determine the LSPR wavelength. We then transferred this experimental method to grow AuNS on GO nanosheets bonded to the PA membrane surface. A laser extinction of 808 nm was used in this work to closely match the determined wavelength of the AuNS (820 nm, Supporting Information Figure S1). These membranes were then exposed to a 2 mM thiol−PEG solution for 3 h to modify the surface of the AuNS with PEG functionalization and to achieve the fully modified PA−GO−AuNS−PEG membrane substrate.

2.3. Membrane Surface Characterization. The membrane surface structure before and after reaction was characterized using scanning electron microscopy (SEM, FEI Nova 2300 field emission, NE), Raman spectroscopy (inVia Raman Microscope, Renishaw), and X-ray photoelectron spectroscopy (XPS, PHI 5000 VersaProbe II, Ulvac-PHI). The membrane surfaces were sputtered with a Au−Pd target for 90 s prior to SEM analysis, and a 10 kV voltage setting was used for all characterizations. For XPS measurements, an Al Kα monochromator radiation was used to measure O 1s and C 1s spectra for PA, PA−GO, and PA−GO−AuNS−PEG membranes with a passing energy of 1486.6 eV. Differences in PA and each modified PA membrane surface layer hydrophilicity, as well as calcite and gypsum hydrophilicity, were determined using contact angle measurements by a contact angle analyzer (Phoenix-300, SEO Co., Ltd., Korea). Freshly cleaved calcite and gypsum coupons were sonicated with acetone for 5 min, rinsed with DI water, and then dried with high purity N_2 gas prior to contact angles measurements. To determine the effect of each membrane modification on membrane surface roughness, atomic force microscopy (AFM, Nanoscope V Multimode SPS, Veeco) was used to image and analyze the PA, PA−GO, PA−GO−AuNS, and PA−GO−AuNS−PEG membranes. The Nanoscope 7.20 software was used to analyze topographic features. Contact angle measurements were conducted using 0.5 M NaCl instead of water to provide insight into the membrane surface properties under the same experimental conditions as the fouling experiments (discussed later). Membrane surface charge was simulated using ground polyamide and PEG-coated polyamide pellets (50−160 μm, Sigma-Aldrich, MO). Because the charged groups on the PA surface are bound to GO, we used the surface charge of aqueous GO to estimate the PA−GO membrane surface charge. Similarly, while we could not accurately determine the surface charge of the PA−GO−AuNS−PEG membrane surface, we assume that it has a surface charge akin to the PA−PEG membrane surface as both are PEGylated.

2.4. Mineral Scaling and Organic Fouling Batch Experiments. To investigate mineral scaling, solutions of potentially nucleating $CaCO_3$ or $CaSO_4$ in a 0.5 M NaCl solution (mimicking brackish RO feed salinities)[46] were injected at the top of batch reactors containing membranes. The reactors were then inverted to study heterogeneous nucleation only (i.e., the membranes were floating on top of solution). After 2 h, membranes were washed with ultrapure DI water for further analyses. The saturation index (SI, log-based), calculated using Geochemist's Workbench (GWB, release 8.0, RockWare, Inc.), with respect to the calcite $CaCO_3$ polymorph formation at the above conditions is 2.16, and with respect to the $CaSO_4$ gypsum polymorph is 0.45. These saturation indices can be found in both natural aqueous systems and water treatment systems,[47,48] and we also considered the faster nucleation kinetics of $CaSO_4$ compared to that of $CaCO_3$.

To study organic fouling on the PA and the PA−GO−AuNS−PEG membrane, we used a semiquantitative approach by measuring and comparing the amount of chemically dyed humic acid present on the membrane surfaces using a CRAIC microspectrophotometer (QDI 302) coupled to a Leica optical microscope (DM 4000 M). First, a 25 mg/L humic acid in 0.5 M NaCl solution was prepared and stirred overnight. For visualization and quantification of the humic acid interaction with membrane surfaces, after mixing, a toluidine blue o (TBO) dye powder was added to form a 1% TBO solution and stain the humic acid. TBO is a cationic dye which at high pH will bind to deprotonated functional groups such as carboxyl and hydroxyl groups.[49] The pH of this mixture was raised to 8.5 to make the humic acid more soluble and ensure TBO binding to the humic acid functional groups.[50] After stirring for 8 h, the TBO bound humic acid solution was filtered through a 0.2 μm syringe filter. The PA and PA−GO−AuNS−PEG membranes were prepared in the same manner as the mineral scaling experiments with the TBO bound humic acid solution being introduced, and then the sample cell was inverted to prevent gravitational accumulation of humic acid on the membrane surface and to investigate the chemical interactions between humic acid and membrane surfaces. After 4 h of contact with the TBO bound humic acid solution, the membranes were rinsed with a 50 v/v% acetic acid solution (pH 2) to remove excess TBO that was not bound to humic acid on the membrane surface. Then, the membranes were measured with a CRAIC microspectrophotometer with 10 accumulations and 0.1 s exposure time in reflection mode. A scan range at wavelengths 400−800 nm measures extinction of the TBO bound humic acid present on the membrane surfaces as TBO absorbs at approximately 630 nm. To determine a baseline for extinction measurements, PA and PA−GO−AuNS−PEG membranes were also measured using the CRAIC microspectrophotometer in the absence of humic acid.

2.5. Membrane Temperature Profile Measurements and Photothermal Efficiency Tests against *Escherichia coli*. Temperature profiles were measured for each membrane layer modification using the 808 nm wavelength near-infrared (NIR) laser to determine photothermal functionality. A near-infrared (NIR) camera is placed 7 cm away from the membrane, which records the temperature 3−5 °C less than the actual membrane temperature. Each of the membranes, PA, PA−GO, PA−PEG, and PA−GO−AuNS−PEG, were exposed to an 808 nm laser at a power of 700 mW/cm^2. For biofouling experiments, an *E. coli* MG1655 was grown in Luria−Bertani liquid medium at 37 °C. All cultivations were in 125 mL baffled shake flasks (25 mL working volume, shaking at 225 rpm). The exponential growing cells (>10^8 live cells/mL) were harvested after 12 h of incubation and then used for photothermal treatment. A layer of MG1655 *E. coli* biofilm was grown on the membrane surfaces, and then exposed to a NIR laser (808 nm) for 10 min at 400 mW/cm^2. The 400 mW/cm^2 power was used to test the PA−GO−AuNS−PEG membrane bactericidal activity to demonstrate the efficacy of the multifunctional membranes at even lower power. After photothermal treatment, the biofilm was exposed to florescent dyes (Molecular Probes Live/Cell Bacterial cell viability kit) for 20 min, and then imaged with a Leica microscope to identify live cells (blue fluorescent filter, 340−380 nm) and dead cells (green fluorescent filter, 450−490 nm).

DOI: 10.1021/am509174j
ACS Appl. Mater. Interfaces 2015, 7, 11117−11126

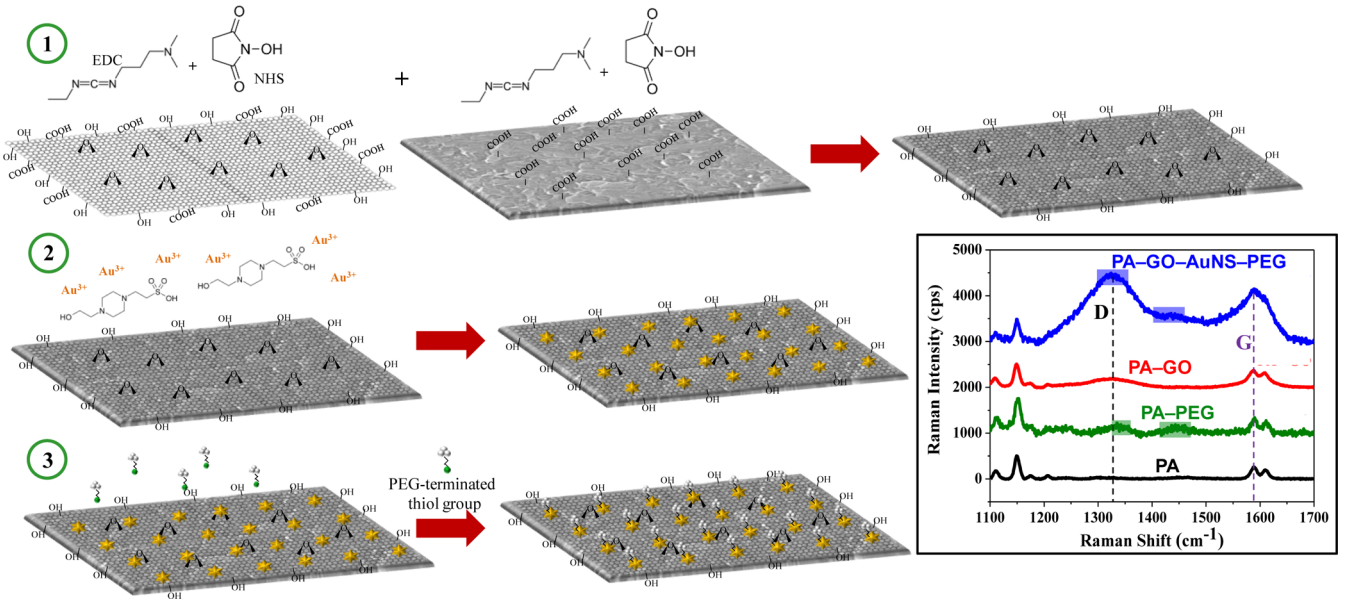

Figure 1. Schematic of membrane fabrication steps used to generate the multifunctional membranes. In step 1, EDC and NHS are used to activate functional groups in the GO and PA to bond nanosheets to the membrane surface. In step 2, $HAuCl_4$ and HEPES are added in solution to initiate growth of AuNS on the PA−GO membrane. Finally, in step 3, SH-PEG groups are drop-casted onto the membrane to covalently bind PEG to the AuNS surface. The boxed inset in the figure contains Raman spectra of each membrane surface modification with indicated graphitic G- and defect D-bands.

2.6. Membrane Flux and Rejection Tests Using a Benchtop RO System. To determine how the membrane surface modifications of GO, AuNS, and PEG affect the membrane performance under RO operating conditions, a Sterlitech CF042 (membrane surface area of 42 cm^2) crossflow benchtop RO system was utilized. Membrane performances were measured by testing permeate water flux and salt rejection. A schematic of the RO configuration is provided in the Supporting Information (Figure S2). A hydraulic piston pump (115/230 VAC, Cole Parmer) was used to first open membrane pores by flowing through DI water at 250 psi for 12 h before the addition of foulants. Three reaction systems were examined to determine the effects of the proposed membrane surface modifications on membrane performance: (1) 10 mM NaCl, (2) 10 mM NaCl + $CaSO_4$ (gypsum SI = −0.05), and (3) 10 mM NaCl + 10 mg/L humic acid. The NaCl concentration is in the range of NaCl concentrations used by others to investigate membrane flux and salt rejection.[42,45,51−53] To initiate $CaSO_4$ formation in system 2, Na_2SO_4 and $CaCl_2$ salts were added to the feed solution at concentrations of 0.02 and 0.03 M, respectively. This gypsum saturation index was selected because it can be found in RO feed waters,[54] and can help elucidate trends in fouling experiments. The salt concentrations are also similar to concentrations used by others to investigate gypsum fouling on RO membranes.[8,9,55] In system 3, humic acid was added to the feed solution to make a 10 mg/L humic acid solution. This humic acid concentration is in the range of NOM concentrations in RO feed waters,[56] and concentrations used by other researchers investigating NOM fouling.[11,57] The permeate was collected over a period of 4 h using a fraction collector and the salt rejection measured using a Ca^{2+} and/or Cl^- ion selective electrode (Thermo Scientific). To determine humic acid rejection, samples were analyzed using a total organic carbon (TOC) analyzer (Shimadzu TOC-LCPH, Kyoto Japan). For visualization of the extent of fouling on membranes, SEM images were taken of membrane surfaces after the fouling experiments to compare the degree of fouling on PA and PA−GO−AuNS−PEG membranes for each system.

3. RESULTS AND DISCUSSION

3.1. Synthesis of Multifunctional Membranes. A novel set of materials was used to generate the new multifunctional RO membrane (fabrication steps illustrated in Figure 1). Commercially available TFC membranes were first chemically modified with GO, a 2D honeycomb-structured nanosheet.[58] In addition to possessing inherent photothermal[59] and bactericidal activity,[60] GO facilitates the *in situ* Au nanostar growth on the membrane surface. The AuNS grown on these GO-membranes (PA−GO) provide even stronger photothermal functionality. Due to strong absorption at the LSPR wavelength,[30,61,62] AuNS are highly effective photothermal agents in the near IR (NIR) range.[29] Furthermore, the star shape absorbs light more than Au nanospheres.[29]

SEM and TEM micrographs (Figure 2) show the progression of membrane functionalization, while Raman spectra (Figure 1, inset) provide further evidence of surface modification. SEM also indicates a uniform distribution of AuNS on the membrane. While the hydrophilic PEG layer cannot be visualized using SEM, the 19° reduction in contact angle (from the innate PA surface) indicated successful binding of PEG (Table 1). The shaded Raman bands at 1347 and 1462 cm^{-1} associated with the C−H vibrations in the PEG structure[63] further confirm the successful PEG binding to the PA membrane surface. In the Raman spectra (Figure 1, inset), the defect-band (D) at 1360 cm^{-1}, associated with graphitic carbon structures,[64] confirms GO on the membrane surface. In the PA−GO−AuNS−PEG membrane, the plasmonic AuNS on the membrane surface enhanced the Raman signal (particularly the G- and D-bands)[65] due to the increased electromagnetic field at the AuNS surface. The XPS spectra (Supporting Information Figure S3) also reveal an increase in oxygen content from the PA, to PA−GO, to PA−GO−AuNS−PEG membranes from 24.5%, to 29.1%, to 32.1%, respectively, providing evidence of successful bonding of hydroxyl and epoxide GO groups,[37] and, subsequently, PEG monomers on the membrane surfaces.[18]

3.2. Resistance against Inorganic Foulants. $CaCO_3$ and $CaSO_4$ mineral scaling on each membrane (Figure 3) indicated increasing fouling resistance as follows: PA−GO < PA < PA−

DOI: 10.1021/am509174j
ACS Appl. Mater. Interfaces 2015, 7, 11117−11126

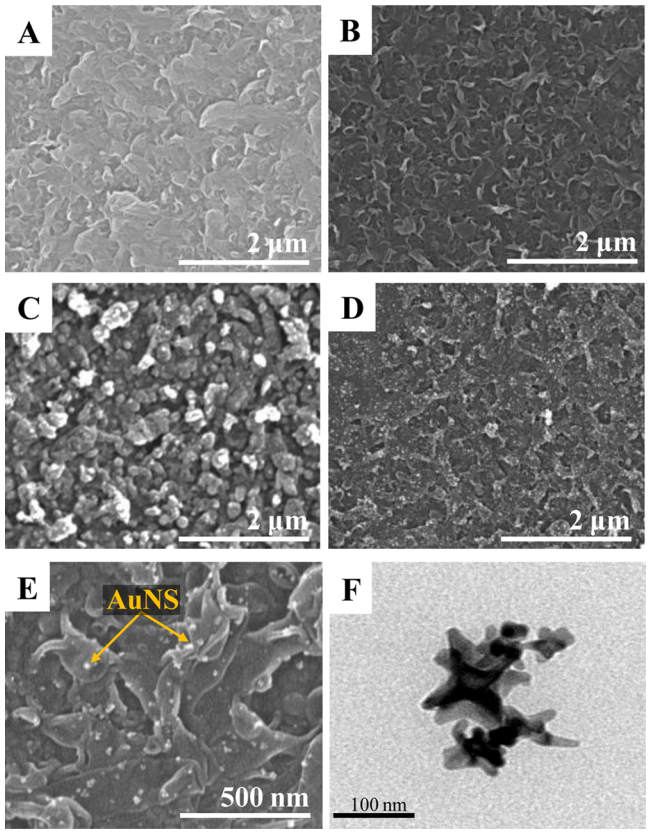

Figure 2. SEM micrographs of (A) PA, (B) PA–GO, (C) PA–PEG, (D) PA–GO–PEG–AuNS, and (E) magnified PA–GO–PEG–AuNS membrane surfaces. The transmission electron microscope inset of Au nanostars removed from the PA–GO–PEG–AuNS membrane surface during sonication in double-filtered water in part F confirms the nanostar structure exists on the membrane surface.

Table 1. Summary of Surface Charges and Contact Angles of Membranes and Ca Salt Minerals[a]

material	contact angle	surface charge (mV)
$CaCO_3$	15.02 ± 0.01°	−7.0 ± 1.9
$CaSO_4$	8.4 ± 0.2°	−4.5 ± 0.3
PA	36.4 ± 0.3°	−6.9 ± 2.3
PA–GO	33.6 ± 0.7°	−14.5 ± 1.7
PA–PEG	14.5 ± 0.1°	0.6 ± 0.2
PA–GO–AuNS–PEG	17.8 ± 0.4°	∼0

[a]Contact angle measurements were measured using a 0.5 M NaCl solution to determine substrate surface hydrophilicity at the experimental conditions of the batch reactor conditions.

PEG < PA–GO–AuNS–PEG. Membrane surface contact angle and surface charge analyses elucidate scaling mechanisms (summarized in Table 1). First, surface hydrophilicity based on contact angle measurements was tested as a potential dominant scaling mechanism. PA and PA–GO membrane surfaces had larger 0.5 M NaCl solution contact angles (36.4° for PA and 33.6° for PA–GO) than those of the PA–PEG and PA–GO–AuNS–PEG membrane surfaces (14.5° and 17.8°, respectively). For both Ca^{2+} salts (contact angles of 15.02° for $CaCO_3$ and 8.4° for $CaSO_4$), scaling is favored on the PA and PA–GO membrane surfaces, and inhibited on the PA–PEG and PA–GO–AuNS–PEG membrane surfaces. This suggests that membrane surface hydrophilicity may not be a dominant mechanism for controlling both $CaCO_3$ and $CaSO_4$ scaling.

Next, we investigated electrostatic interactions based on surface charge measurements to provide more insight into mineral scaling resistance mechanisms (Table 1). The PA and PA–GO membrane surfaces are negatively charged, while both PEG-modified membrane surfaces have a circumneutral charge due to the uncharged PEG monomer.[44] In this work, we assume that, due to the PEG functionality, the PA–GO–AuNS–PEG membrane surface has a circumneutral charge similar to the PA–PEG surface charge as well. Thus, the negatively charged membrane surfaces should be more effective in attracting positively charged Ca^{2+} ions for nucleation than the uncharged surfaces.[8] As Table 1 shows, the PA–GO surface is the most negatively charged (−14.5 mV) and exhibits the most mineral scaling of all membrane surfaces (Figure 3A2,B2). On the basis of this information, we found that membrane surface charge can be an important mechanism in controlling both $CaCO_3$ and $CaSO_4$ scaling, while membrane surface hydrophilicity may be less important in predicting $CaSO_4$ scaling.

Interestingly, the PA–GO–AuNS–PEG membrane surface exhibited the least mineral scaling, with few or no observable precipitates over the reactive surface area (Figure 3A4,B4). There are several possible reasons: First, as previously stated, the neutral charge of PEG bonded to AuNS on the membrane surface should be less effective in attracting Ca^{2+} ions. Second, the PA–PEG is further distinguished from the PA–GO–AuNS–PEG membrane surface by the presence of Au nanostructures. The GO strongly promoted both $CaCO_3$ and $CaSO_4$ scaling (Figure 3A2,B2). Therefore, the AuNS, while also reducing biofouling (discussed later), can help prevent Ca^{2+} salt nucleation. However, there is only limited work investigating the heterogeneous nucleation of $CaCO_3$ and/or $CaSO_4$ crystals on Au nanoparticles. Some researchers have investigated forced nucleation of $CaCO_3$ and $CaSO_4$ crystals via electrochemical deposition on Au particle and substrate surfaces.[66,67] Aizenberg et al. investigated aqueous $CaCO_3$ precipitation in the presence of Au substrates; however, the Au surface had to be functionalized with acid-terminated functional groups to promote $CaCO_3$ nucleation.[68] Results from an additional mineral scaling test on a Au-sputtered PA membrane (Supporting Information Figure S4) indicated significant inhibition of scaling due to the Au coating on the membrane, which supports our observations of negligible scaling on the PA–GO–AuNS–PEG membranes.

Membrane surface roughness may also contribute to mineral scaling. According to literature studies, fouling worsens in the presence of membrane surfaces with a higher surface roughness due to attractive DLVO interactions between foulants and the active membrane surface layer.[69−71] In our study, the surface roughness root-mean-square values over a 4 μm × 4 μm area of the PA, PA–GO, PA–GO–AuNS, and PA–GO–AuNS–PEG membrane were 57.4, 33.4, 78.7, and 61.4 nm, respectively. The grafting of GO to the membrane surface will reduce surface roughness.[72,73] The presence of star-shaped Au nanoparticles then significantly increases the surface roughness, and then the subsequent binding of PEG monomers will slightly smooth the surface. On the basis of our surface roughness analyses using atomic force microscopy, the PA and PA–GO membrane surface should exhibit the least amount of fouling; however, the mineral scaling analysis indicates that these membranes attract more $CaCO_3$ and $CaSO_4$ pre-nucleation clusters than the PA–GO–AuNS–PEG membrane. Furthermore, the results from the additional mineral scaling test (Supporting Information

DOI: 10.1021/am509174j
ACS Appl. Mater. Interfaces 2015, 7, 11117−11126

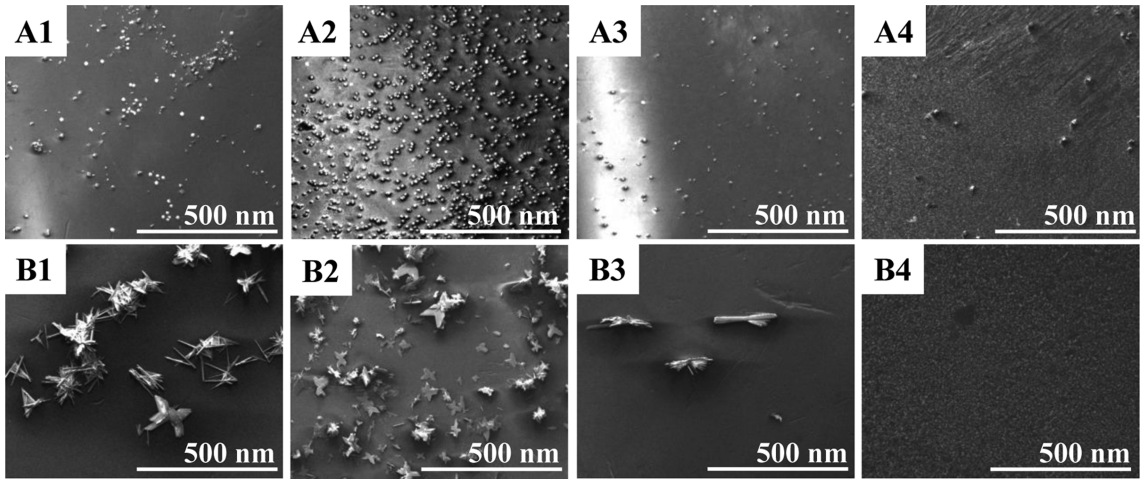

Figure 3. SEM micrographs of $CaCO_3$ (row A) and $CaSO_4$ (row B) mineral scaling experiments on the (1) PA (commercially available membrane), (2) PA–GO, (3) PA–PEG, and (4) PA–GO–AuNS–PEG membrane surfaces.

Figure S4) revealed that AuNS significantly inhibit scaling on the AuNS-modified membrane surfaces despite them having the largest surface roughness. Therefore, the membrane surface roughness fouling enhancement is negligible in our experimental membrane systems.

3.3. Resistance against Organic Foulants. The multifunctional membranes also significantly reduced organic fouling (Figure 4 and Supporting Information Figure S5). While

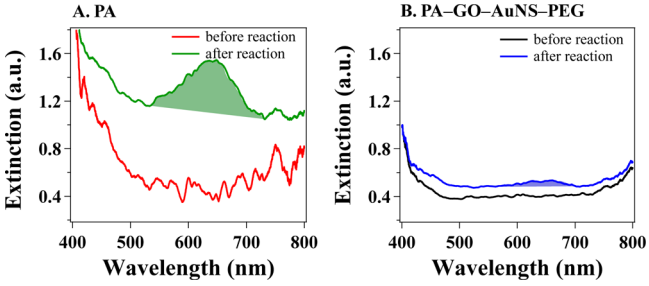

Figure 4. (A) Extinction spectra of PA and (B) PA–GO–AuNS–PEG membranes before and after reaction with TBO-stained humic acid solutions.

deposition on the PA–GO–AuNS–PEG membrane surface was low as indicated by the small 630 nm peak (TBO absorption peak)[74] (Figure 4B), there was a large increase in the 630 nm peak after reaction with humic acid on the PA membrane surface (Figure 4A). The peak area is proportional to the extents of TBO bound humic acid on membranes. Thus, the comparison of peak areas from these membrane systems can provide semi-quantitative information on humic acid fouling resistance on membranes. In previous studies, polyamide on the TFC surface has been shown to readily adsorb humic acid during fouling experiments.[75,76] In addition, GO can effectively sorb natural organic matter.[77] In PA–GO–AuNS–PEG membranes, however, AuNS can inhibit organic matter accumulation. In addition, the hydrophilic, uncharged PEG coating can help improve RO membrane flux as well as organic fouling resistance[42,78] most likely due to repulsion between the hydrophilic membrane surface and the hydrophobic humic acid.

3.4. Resistance against Biofoulants. Finally, photothermal bacterial lysis on the membrane surface was tested, which has not been reported previously to the best of our knowledge. Because photothermal treatment is generally performed in solution (3-dimensional contact), we used spiked plasmonic nanostructures (Figure 2F) with the highest possible photothermal conversion efficiency[79] (achieved by tuning AuNS absorption to 808 nm) to compensate for the 2-dimensional treatment. This resulted in steeper temperature profiles (Figure 5) in our study than predicted for Au

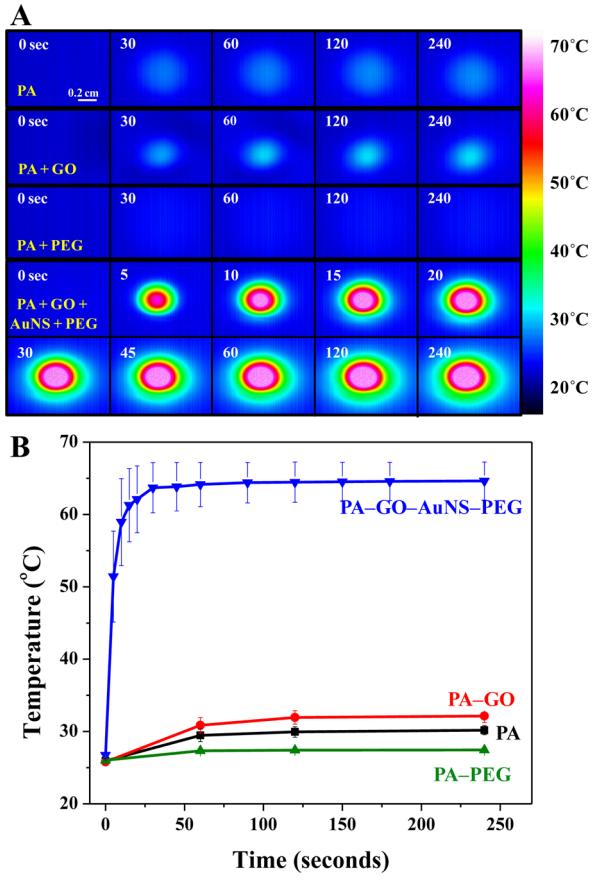

Figure 5. (A) NIR camera images of PA, PA–GO, PA–PEG, and PA–GO–AuNS–PEG membranes with time, and (B) the corresponding temperature profiles.

DOI: 10.1021/am509174j
ACS Appl. Mater. Interfaces 2015, 7, 11117–11126

nanorods.[59] The PA membranes did not show a significant temperature rise as the temperature raise is associated with radiative heat transfer. The PA−PEG membrane showed a drop in the temperature, possibly due to PEG absorbing water[80] which could decrease the local temperature on the membrane surface and scatter more light compared to the TFC composite membrane. The PA−GO membrane showed a slight rise in temperature to 35 °C because of the photothermal properties of graphene oxide.[59] The actual temperature on the membrane PA−GO−AuNS−PEG reaches around 70 °C in 50 s and stays constant for longer laser exposure times. It is worth noting that the membrane did not degrade for 10 min upon exposure to the laser.

To test bacterial inactivation capabilities, the PA−GO−AuNS−PEG membrane was covered with a layer of *E. coli*. Cell walls of *E. coli* are reported to deteriorate at temperatures near 70 °C.[59] To prove the superior effectiveness of our multifunctional membranes, a lower laser power (400 mW/cm^2) than reported previously[81] was used. In Figure 6, the PA membrane

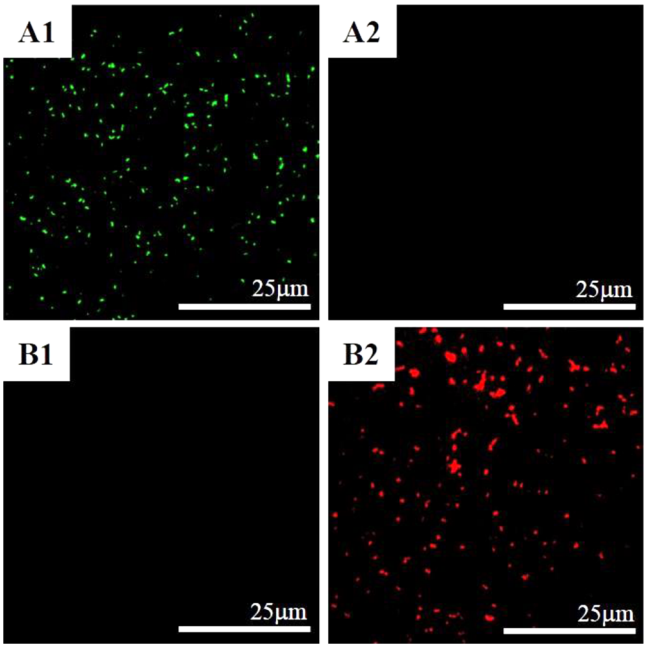

Figure 6. *E. coli* fluorescence images of (A) PA and (B) PA−GO−AuNS−PEG membranes indicating (column 1) live and (column 2) dead cells after 10 min of exposure of a 400 mW/cm^2 power NIR source.

showed green florescence (i.e., live bacteria), while the PA−GO−AuNS−PEG membrane was treated using 600 s of 400 mW/cm^2 laser power showed only red stains (i.e., dead bacteria) in Figure 6, which demonstrates that photothermal capability can be achieved in RO systems using these membranes. SEM images also indicate deterioration of bacteria cell walls after treatment (Supporting Information Figure S6). In future large-scale RO applications, these membranes can be illuminated by multiple light sources (e.g., a low cost light emitting diode assembly) to significantly reduce the required illumination time and immediately kill bacteria.

3.5. RO Membrane Performance. To determine the viability and efficacy of the multifunctional membrane in RO systems, the PA and PA−GO−AuNS−PEG membranes were tested for permeate water flux and rejection for (1) 10 mM NaCl (Supporting Information Figure S7), (2) 10 mM NaCl + $CaSO_4$, and (3) 10 mM NaCl + 10 mg/L HA feed solutions (Figure 7). For the 10 mM NaCl feed, the measured water flux

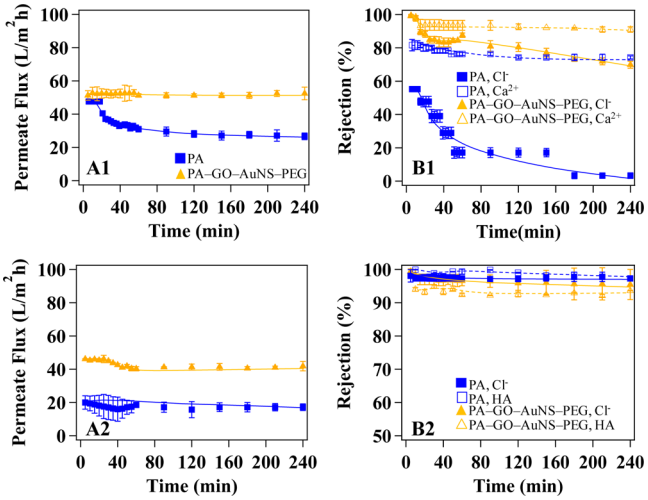

Figure 7. (A) Test results of permeate flux and (B) rejection of PA and PA−GO−AuNS−PEG membranes in (1) model $CaSO_4$ foulant (10 mM NaCl + $CaSO_4$; gypsum, SI = −0.05) and (2) model natural organic matter foulant (10 mM NaCl + 10 mg/L HA) feed solutions as a function of time.

and Cl^- rejection of the PA membrane were comparable with reports of other work investigating polyamide thin film composite membrane fouling under similar conditions (Supporting Information Figure S7).[42,52,53,82,83] Furthermore, the permeate flux and salt rejection of the PA−GO−AuNS−PEG membranes were similar to those from the PA membrane in our study. For the permeate flux, initially, the PA flux is higher than the flux of the multifunctional membrane surface. However, there is a rapid decrease in flux over time as the membrane efficacy decays. The permeate flux of the PA−GO−AuNS−PEG membrane appears to maintain a steady-state flux over the 4 h reaction period. For the 10 mM NaCl + $CaSO_4$ system, the Ca^{2+} and Cl^- salt rejection through the PA−GO−AuNS−PEG membranes is significantly higher compared to the PA membrane (Figure 7B1) and the flux is almost 50% higher (Figure 7A1). The SEM analysis indicates that gypsum formation on the PA−GO−AuNS−PEG membrane is negligible compared to the extensive scale formation on the PA membrane, which supports the flux and rejection analysis (Supporting Information Figure S8). For the humic acid rejection (Figure 7B2), the performance from the PA membrane and the PA−GO−AuNS−PEG membrane are similar (a rejection of 97% over 94%, respectively); however, the flux for the PA−GO−AuNS−PEG membrane is almost 2.5 times higher than that for the PA membrane (Figure 7A2). Therefore, overall, the performance of the PA−GO−AuNS−PEG membrane is superior to the PA membrane performance, and the membrane surface modifications in this study did not significantly reduce membrane performance.

4. CONCLUSION

For the first time, we have demonstrated a unique, synergistic multifunctional membrane that significantly eliminates mineral scaling, organic fouling, and biofouling for optimized RO membrane performance. By taking advantage of AuNS

DOI: 10.1021/am509174j
ACS Appl. Mater. Interfaces 2015, 7, 11117−11126

photothermal functionality, we have demonstrated capabilities for bacterial lysis without additional chemical or thermal treatment. We have further demonstrated that the multifunctional PA−GO−AuNS−PEG membranes possess improved salt rejection and water flux to PA membranes in a model benchtop RO system. The proof-of-concept information from this work can be beneficial for designing more efficient, low energy RO systems in which the membrane surface is regenerated during operation. Future directions from this work should include membrane salt rejection and water flux tests in the presence of the model foulants used in this work to examine the efficacy of these membranes in complex RO feeds. The novel multifunctionality achieved in this newly developed membrane shows promising results to drastically improve desalination processes.

■ ASSOCIATED CONTENT

Supporting Information

LSPR wavelength spectra and TEM images of AuNS (Figure S1), schematic diagram of the benchtop RO system (Figure S2), XPS spectra of select membranes (Figure S3), mineral scaling on Au-sputtered membranes (Figure S4), TEM micrographs of organic-fouled membranes (Figure S5), SEM images of treated *E. coli* (Figure S6), 10 mM NaCl membrane fouling flux and rejection results (Figure S7), and SEM images of membranes after fouling experiments (Figure S8). The Supporting Information is available free of charge on the ACS Publications website at DOI: 10.1021/am509174j.

■ AUTHOR INFORMATION

Corresponding Authors

*E-mail: singamaneni@wustl.edu. Phone: (314) 935-5407 Fax: (314) 935-4014.

*E-mail: ysjun@seas.wustl.edu. Phone (314) 935-4539. Fax: (314) 935-7211.

Author Contributions

J.R.R. and S.T. contributed equally.

Notes

The authors declare no competing financial interest.

■ ACKNOWLEDGMENTS

This work is supported by Y.-S.J.'s Washington University Faculty Start-up Grant and NSF Environmental Chemical Science (CHE-1214090) Grant, S.S.'s National Science Foundation CAREER Award (CBET-1254399), and J.R.R.'s Environmental Protection Agency STAR Fellowship. This work was also partially supported from Washington University's International Center for Advanced Renewable Energy & Sustainability (I-CARES). We would like to thank Prof. Lihong Wang for providing the NIR camera used in this study. We would also like to thank Mr. Haesung Jung for his help running XPS measurements.

■ REFERENCES

(1) Elimelech, M.; Phillip, W. A. The Future of Seawater Desalination: Energy, Technology, and the Environment. *Science* **2011**, *333*, 712−717.

(2) Yip, N. Y.; Tiraferri, A.; Phillip, W. A.; Schiffman, J. D.; Elimelech, M. High Performance Thin-Film Composite Forward Osmosis Membrane. *Environ. Sci. Technol.* **2010**, *44*, 3812−3818.

(3) Crittenden, J. C.; Trussell, R. R.; Hand, D. W.; Howe, K. J.; Tchobanoglous, G. *Water Treatment: Principles and Design*, 2nd ed.; John Wiley & Sons, Inc.: New York, 2005.

(4) Subramani, A.; Hoek, E. M. V. Biofilm Formation, Cleaning, Re-Formation on Polyamide Composite Membranes. *Desalination* **2010**, *257*, 73−79.

(5) Wang, Y.-N.; Tang, C. Y. Fouling of Nanofiltration, Reverse Osmosis, and Ultrafiltration Membranes by Protein Mixtures: The Role of Inter-Foulant-Species Interaction. *Environ. Sci. Technol.* **2011**, *45*, 6373−6379.

(6) Zhu, X.; Elimelech, M. Colloidal Fouling of Reverse Osmosis Membranes: Measurements and Fouling Mechanisms. *Environ. Sci. Technol.* **1997**, *31*, 3654−3662.

(7) Greenlee, L. F.; Lawler, D. F.; Freeman, B. D.; Marrot, B.; Moulin, P. Reverse Osmosis Desalination: Water Sources, Technology, and Today's Challenges. *Water Res.* **2009**, *43*, 2317−2348.

(8) Duan, W.; Dudchenko, A.; Mende, E.; Flyer, C.; Zhu, X.; Jassby, D. Electrochemical Mineral Scale Prevention and Removal on Electricity Conducting Carbon Nanotube-Polyamide Reverse Osmosis Membranes. *Environ. Sci.: Processes Impacts* **2014**, *16*, 1300−1308.

(9) Shih, W.-Y.; Rahardianto, A.; Lee, R.-W.; Cohen, Y. Morphometric Characterization of Calcium Sulfate Dihydrate (Gypsum) Scale on Reverse Osmosis Membranes. *J. Membr. Sci.* **2005**, *252*, 253−263.

(10) Bersillon, J. L. Fouling Analysis and Control. In *Future Industrial Prospects of Membrane Processes*; Cécille, L., Toussaint, J. C., Eds.; Elsevier: New York, 1988; pp 234−247.

(11) Hong, S.; Elimelech, M. Chemical and Physical Aspects of Natural Organic Matter (Nom) Fouling of Nanofiltration Membranes. *J. Membr. Sci.* **1997**, *132*, 159−181.

(12) Lee, S.; Elimelech, M. Relating Organic Fouling of Reverse Osmosis Membranes to Intermolecular Adhesion Forces. *Environ. Sci. Technol.* **2006**, *40*, 980−987.

(13) Diagne, F.; Malaisamy, R.; Boddie, V.; Holbrook, R. D.; Eribo, B.; Jones, K. L. Polyelectrolyte and Silver Nanoparticle Modification of Microfiltration Membranes to Mitigate Organic and Bacterial Fouling. *Environ. Sci. Technol.* **2012**, *46*, 4025−4033.

(14) Herzberg, M.; Elimelech, M. Biofouling of Reverse Osmosis Membranes: Role of Biofilm-Enhanced Osmotic Pressure. *J. Membr. Sci.* **2007**, *295*, 11−20.

(15) Khan, M. T.; de O. Manes, C.-L.; Aubry, C.; Gutierrez, L.; Croue, J. P. Kinetic Study of Seawater Reverse Osmosis Membrane Fouling. *Environ. Sci. Technol.* **2013**, *47*, 10884−10894.

(16) Hilal, N.; Kochkodan, V.; Al-Khatib, L.; Levadna, T. Surface Modified Polymeric Membranes to Reduce (Bio)Fouling: A Microbiological Study Using E. Coli. *Desalination* **2004**, *167*, 293−300.

(17) Lee, S. Y.; Kim, H. J.; Patel, R.; Im, S. J.; Kim, J. H.; Min, B. R. Silver Nanoparticles Immobilized on Thin Film Composite Polyamide Membrane: Characterization, Nanofiltration, Antifouling Properties. *Polym. Adv. Technol.* **2007**, *18*, 562−568.

(18) Kang, G.; Liu, M.; Lin, B.; Cao, Y.; Yuan, Q. A Novel Method of Surface Modification on Thin-Film Composite Reverse Osmosis Membrane by Grafting Poly(Ethylene Glycol). *Polymer* **2007**, *48*, 1165−1170.

(19) Kim, J.-H.; Park, P.-K.; Lee, C.-H.; Kwon, H.-H. Surface Modification of Nanofiltration Membranes to Improve the Removal of Organic Micro-Pollutants (Edcs and Phacs) in Drinking Water Treatment: Graft Polymerization and Cross-Linking Followed by Functional Group Substitution. *J. Membr. Sci.* **2008**, *321*, 190−198.

(20) Kwak, S.-Y.; Kim, S. H.; Kim, S. S. Hybrid Organic/Inorganic Reverse Osmosis (Ro) Membrane for Bactericidal Anti-Fouling. 1. Preparation and Characterization of TiO_2 Nanoparticle Self-Assembled Aromatic Polyamide Thin-Film-Composite (Tfc) Membrane. *Environ. Sci. Technol.* **2001**, *35*, 2388−2394.

(21) Rahaman, M. S.; Therien-Aubin, H.; Ben-Sasson, M.; Ober, C. K.; Nielsen, M.; Elimelech, M. Control of Biofouling on Reverse Osmosis Polyamide Membranes Modified with Biocidal Nanoparticles and Antifouling Polymer Brushes. *J. Mater. Chem. B* **2014**, *2*, 1724−1732.

(22) Akhavan, O.; Ghaderi, E. Photocatalytic Reduction of Graphene Oxide Nanosheets on TiO_2 Thin Film for Photoinactivation of

DOI: 10.1021/am509174j
ACS Appl. Mater. Interfaces 2015, 7, 11117−11126

Bacteria in Solar Light Irradiation. *J. Phys. Chem. C* **2009**, *113*, 20214−20220.
(23) Sheet, I.; Holail, H.; Olama, Z.; Kabbani, A.; Hines, M. The Antibacterial Activity of Graphite Oxide, Silver, Impregnated Graphite Oxide with Silver and Go-Coated Sand Nanoparticles against Waterborne Pathogenic E.Coli Bl21. *Int. J. Curr. Microbiol. Appl. Sci.* **2013**, *2*, 1−11.
(24) Gurunathan, S.; Han, J. W.; Dayem, A. A.; Eppakayala, V.; Kim, J. H. Oxidative Stress-Mediated Antibacterial Activity of Graphene Oxide and Reduced Graphene Oxide in Psuedomonas Aeruginosa. *Int. J. Nanomed.* **2012**, *7*, 5901−5914.
(25) Murugan, V.; Linghe, Z.; Karthikeyan, K.; Kyusik, Y. Surface Activation of Graphene Oxide Nanosheets by Ultraviolet Irradiation for Highly Efficient Anti-Bacterials. *Nanotechnology* **2013**, *24*, 395706.
(26) Huang, X.; El-Sayed, I. H.; Qian, W.; El-Sayed, M. A. Cancer Cell Imaging and Photothermal Therapy in the near-Infrared Region by Using Gold Nanorods. *J. Am. Chem. Soc.* **2006**, *128*, 2115−2120.
(27) O'Neal, D. P.; Hirsch, L. R.; Halas, N. J.; Payne, J. D.; West, J. L. Photo-Thermal Tumor Ablation in Mice Using near Infrared-Absorbing Nanoparticles. *Cancer Lett.* **2004**, *209*, 171−176.
(28) Huang, X.; Jain, P.; El-Sayed, I.; El-Sayed, M. Plasmonic Photothermal Therapy (Pptt) Using Gold Nanoparticles. *Lasers Med. Sci.* **2008**, *23*, 217−228.
(29) Nergiz, S. Z.; Gandra, N.; Singamaneni, S. Self-Assembled High Aspect Ratio Gold Nanostar/Graphene Oxide Hybrid Nanorolls. *Carbon* **2014**, *66*, 585−591.
(30) Jain, P. K.; Huang, X.; El-Sayed, I. H.; El-Sayed, M. A. Noble Metals on the Nanoscale: Optical and Photothermal Properties and Some Applications in Imaging, Sensing, Biology, and Medicine. *Acc. Chem. Res.* **2008**, *41*, 1578−1586.
(31) Hutter, E.; Fendler, J. H. Exploitation of Localized Surface Plasmon Resonance. *Adv. Mater.* **2004**, *16*, 1685−1706.
(32) Jain, P. K.; Huang, X. H.; El-Sayed, I. H.; El-Sayed, M. A. Noble Metals on the Nanoscale: Optical and Photothermal Properties and Some Applications in Imaging, Sensing, Biology, and Medicine. *Acc. Chem. Res.* **2008**, *41*, 1578−1586.
(33) Link, S.; El-Sayed, M. A. Optical Properties and Ultrafast Dynamics of Metallic Nanocrystals. *Annu. Rev. Phys. Chem.* **2003**, *54*, 331−366.
(34) Yamada, K.; Miyajima, K.; Mafune, F. Thermionic Emission of Electrons from Gold Nanoparticles by Nanosecond Pulse-Laser Excitation of Interband. *J. Phys. Chem. C* **2007**, *111*, 11246−11251.
(35) Hashimoto, S.; Werner, D.; Uwada, T. Studies on the Interaction of Pulsed Lasers with Plasmonic Gold Nanoparticles toward Light Manipulation, Heat Management, and Nanofabrication. *J. Photochem. Photobiol., C* **2012**, *13*, 28−54.
(36) Norman, R. S.; Stone, J. W.; Gole, A.; Murphy, C. J.; Sabo-Attwood, T. L. Targeted Photothermal Lysis of the Pathogenic Bacteria, Pseudomonas Aeruginosa, with Gold Nanorods. *Nano Lett.* **2007**, *8*, 302−306.
(37) Hu, M.; Mi, B. Enabling Graphene Oxide Nanosheets as Water Separation Membranes. *Environ. Sci. Technol.* **2013**, *47*, 3715−3723.
(38) Lee, J.; Chae, H.-R.; Won, Y. J.; Lee, K.; Lee, C.-H.; Lee, H. H.; Kim, I.-C.; Lee, J.-m. Graphene Oxide Nanoplatelets Composite Membrane with Hydrophilic and Antifouling Properties for Wastewater Treatment. *J. Membr. Sci.* **2013**, *448*, 223−230.
(39) Cohen-Tanugi, D.; Grossman, J. C. Water Desalination across Nanoporous Graphene. *Nano Lett.* **2012**, *12*, 3602−3608.
(40) Freger, V.; Gilron, J.; Belfer, S. Tfc Polyamide Membranes Modified by Grafting of Hydrophilic Polymers: An Ft-Ir/Afm/Tem Study. *J. Membr. Sci.* **2002**, *209*, 283−292.
(41) Kang, G.; Yu, H.; Liu, Z.; Cao, Y. Surface Modification of a Commercial Thin Film Composite Polyamide Reverse Osmosis Membrane by Carbodiimide-Induced Grafting with Poly(Ethylene Glycol) Derivatives. *Desalination* **2007**, *275*, 252−259.
(42) Sagle, A. C.; Van Wagner, E. M.; Ju, H.; McCloskey, B. D.; Freeman, B. D.; Sharma, M. M. Peg-Coated Reverse Osmosis Membranes: Desalination Properties and Fouling Resistance. *J. Membr. Sci.* **2009**, *340*, 92−108.
(43) Sagle, A. C.; Van Wagner, E. M.; Ju, H.; McCloskey, B. D.; Freeman, B. D.; Sharma, M. M. Peg-Coated Reverse Osmosis Membranes: Desalination Properties and Fouling Resistance. *J. Membr. Sci.* **2009**, *340*, 92−108.
(44) Freger, V.; Gilron, J.; Belfer, S. Tfc Polyamide Membranes Modified by Grafting of Hydrophilic Polymers: An Ft-Ir/Afm/Tem Study. *J. Membr. Sci.* **2002**, *209*, 283−292.
(45) Perreault, F.; Tousley, M. E.; Elimelech, M. Thin-Film Composite Polyamide Membranes Functionalized with Biocidal Graphene Oxide Nanosheets. *Environ. Sci. Technol. Lett.* **2014**, *1*, 71−76.
(46) Zou, L.; Li, L.; Song, H.; Morris, G. Using Mesoporous Carbon Electrodes for Brackish Water Desalination. *Water Res.* **2008**, *42*, 2340−2348.
(47) Thompson, J. B.; Ferris, F. G. Cyanobacterial Precipitation of Gypsum, Calcite, and Magnesite from Natural Alkaline Lake Water. *Geology* **1990**, *18*, 995−998.
(48) Zhang, M.; Hou, D.; She, Q.; Tang, C. Y. Gypsum Scaling in Pressure Retarded Osmosis: Experiments, Mechanisms and Implications. *Water Res.* **2014**, *48*, 387−395.
(49) Alpat, S. K.; Ozbayrak, O.; Alpat, S.; Akcay, H. The Adsorption Kinetics and Removal of Cationic Dye, Toluidine Blue O, from Aqueous Solution with Turkish Zeolite. *J. Hazard. Mater.* **2008**, *151*, 213−220.
(50) Yuan, W.; Zydney, A. L. Humic Acid Fouling During Microfiltration. *J. Membr. Sci.* **1999**, *157*, 1−12.
(51) Jin, W.; Toutianoush, A.; Tieke, B. Use of Polyelectrolyte Layer-by-Layer Assemblies as Nanofiltration and Reverse Osmosis Membranes. *Langmuir* **2003**, *19*, 2550−2553.
(52) Lind, M. L.; Ghosh, A. K.; Jawor, A.; Huang, X.; Hou, W.; Yang, Y.; Hoek, E. M. V. Influence of Zeolite Crystal Size on Zeolite-Polyamide Thin Film Nanocomposite Membranes. *Langmuir* **2009**, *25*, 10139−10145.
(53) Van Wagner, E. M.; Sagle, A. C.; Sharma, M. M.; Freeman, B. D. Effect of Crossflow Testing Conditions, Including Feed Ph and Continuous Feed Filtration, on Commercial Reverse Osmosis Membrane Performance. *J. Membr. Sci.* **2009**, *345*, 97−109.
(54) Rahardianto, A.; Gao, J.; Gabelich, C. J.; Williams, M. D.; Cohen, Y. High Recovery Membrane Desalting of Low-Salinity Brackish Water: Integration of Accelerated Precipitation Softening with Membrane Ro. *J. Membr. Sci.* **2007**, *289*, 123−137.
(55) Liu, Y.; Mi, B. Effects of Organic Macromolecular Conditioning on Gypsum Scaling of Forward Osmosis Membranes. *J. Membr. Sci.* **2014**, *450*, 153−161.
(56) Lee, N.; Amy, G.; Croue, J.-P.; Buisson, H. Identification and Understanding of Fouling in Low-Pressure Membrane (Mf/Uf) Filtration by Natural Organic Matter (NOM). *Water Res.* **2004**, *38*, 4511−4523.
(57) Tang, C. Y.; Kwon, Y.-N.; Leckie, J. O. Fouling of Reverse Osmosis and Nanofiltration Membranes by Humic Acid−Effects of Solution Composition and Hydrodynamic Conditions. *J. Membr. Sci.* **2007**, *290*, 86−94.
(58) Gonçalves, G.; Vila, M.; Portolés, M.-T.; Vallet-Regi, M.; Gracio, J.; Marques, P. A. A. P. Nano-Graphene Oxide: A Potential Multifunctional Platform for Cancer Therapy. *Adv. Healthcare Mater.* **2013**, *2*, 1072−1090.
(59) Lim, D.-K.; Barhoumi, A.; Wylie, R. G.; Reznor, G.; Langer, R. S.; Kohane, D. S. Enhanced Photothermal Effect of Plasmonic Nanoparticles Coated with Reduced Graphene Oxide. *Nano Lett.* **2013**, *13*, 4075−4079.
(60) Akhavan, O.; Ghaderi, E. Toxicity of Graphene and Graphene Oxide Nanowalls against Bacteria. *Nano Energy* **2010**, *4*, 5731−5736.
(61) Nam, J.; Won, N.; Jin, H.; Chung, H.; Kim, S. Ph-Induced Aggregation of Gold Nanoparticles for Photothermal Cancer Therapy. *J. Am. Chem. Soc.* **2009**, *131*, 13639−13645.
(62) Bardhan, R.; Lal, S.; Joshi, A.; Halas, N. J. Theranostic Nanoshells: From Probe Design to Imaging and Treatment of Cancer. *Acc. Chem. Res.* **2011**, *44*, 936−946.

DOI: 10.1021/am509174j
ACS Appl. Mater. Interfaces 2015, 7, 11117−11126

(63) Zanini, S.; Riccardi, C.; Orlandi, M.; Colombo, C.; Croccolo, F. Plasma-Induced Graft-Polymerisation of Ethylene Glycol Methacrylate Phosphate on Polyethylene Films. *Polym. Degrad. Stab.* **2008**, *93*, 1158−1163.
(64) Wang, Y.; Alsmeyer, D. C.; McCreery, R. L. Raman Spectroscopy of Carbon Materials: Structural Basis of Observed Spectra. *Chem. Mater.* **1990**, *2*, 557−563.
(65) Ferrari, A. C.; Meyer, J. C.; Scardaci, V.; Casiraghi, C.; Lazzeri, M.; Mauri, F.; Piscanec, S.; Jiang, D.; Novoselov, K. S.; Roth, S.; Geim, A. K. Raman Spectrum of Graphene and Graphene Layers. *Phys. Rev. Lett.* **2006**, *97*, 187401.
(66) Teghidet, H.; Bernard, M. C.; Borensztajn, S.; Chaal, L.; Joiret, S.; Saidani, B. Calcite Epitaxy on Au and Ag (1 1 1). *J. Cryst. Growth* **2011**, *331*, 72−77.
(67) Lee, S.-K.; Lee, M.-K.; Lee, H. Surfactant-Free Synthesis of $Caso_4$ Nanorod/Nanowire by Electrochemical Deposition. *J. Electrochem. Soc.* **2010**, *157*, K43−K46.
(68) Aizenberg, J.; Black, A. J.; Whitesides, G. M. Control of Crystal Nucleation by Patterned Self-Assembled Monolayers. *Nature* **1999**, *398*, 495−498.
(69) Elimelech, M.; Xiaohua, Z.; Childress, A. E.; Seungkwan, H. Role of Membrane Surface Morphology in Colloidal Fouling of Cellulose Acetate and Composite Aromatic Polyamide Reverse Osmosis Membranes. *J. Membr. Sci.* **1997**, *127*, 101−109.
(70) Hoek, E. M. V.; Bhattacharjee, S.; Elimelech, M. Effect of Membrane Surface Roughness on Colloid-Membrane DLVO Interactions. *Langmuir* **2003**, *19*, 4836−4847.
(71) Xu, P.; Drewes, J. E.; Kim, T.-U.; Bellona, C.; Amy, G. Effect of Membrane Fouling on Transport of Organic Contaminants in Nf/Ro Membrane Applications. *J. Membr. Sci.* **2006**, *279*, 165−175.
(72) Choi, W.; Choi, J.; Bang, J.; Lee, J.-H. Layer-by-Layer Assembly of Graphene Oxide Nanosheets on Polyamide Membranes for Durable Reverse-Osmosis Applications. *ACS Appl. Mater. Interfaces* **2013**, *5*, 12510−12519.
(73) Zhao, H.; Wu, L.; Zhou, Z.; Zhang, L.; Chen, H. Improving the Antifouling Property of Polysulfone Ultrafiltration Membrane by Incorporation of Isocyanate-Treated Graphene Oxide. *Phys. Chem. Chem. Phys.* **2013**, *15*, 9084−9092.
(74) Nagata, J. Y.; Hioka, N.; Kimura, E.; Batistela, V. R.; Terada, R. S. S.; Graciano, A. X.; Baesso, M. L.; Hayacibara, M. F. Antibacterial Photodynamic Therapy for Dental Caries: Evaluation of the Photosensitizers Used and Light Source Properties. *Photodiagn. Photodyn.* **2012**, *9*, 122−131.
(75) Tang, C. Y.; Kwon, Y.-N.; Leckie, J. O. Fouling of Reverse Osmosis and Nanofiltration Membranes by Humic Acid: Effects of Solution Composition and Hydrodynamic Conditions. *J. Membr. Sci.* **2007**, *290*, 86−94.
(76) Childress, A. E.; Deshmukh, S. S. Effect of Humic Substances and Anionic Surfactants on the Surface Charge and Performance of Reverse Osmosis Membranes. *Desalination* **1998**, *118*, 167−174.
(77) Apul, O. G.; Wang, Q.; Zhou, Y.; Karanfil, T. Adsorption of Aromatic Organic Contaminants by Graphene Nanosheets: Comparison with Carbon Nanotubes and Activated Carbon. *Water Res.* **2012**, *47*, 1648−1654.
(78) Kang, G.-d.; Cao, Y.-m. Development of Antifouling Reverse Osmosis Membranes for Water Treatment: A Review. *Water Res.* **2012**, *46*, 584−600.
(79) Yuan, H.; Khoury, C. G.; Wilson, C. M.; Grant, G. A.; Bennett, A. J.; Vo-Dinh, T. In Vivo Particle Tracking and Photothermal Ablation Using Plasmon-Resonant Gold Nanostars. *Nanomed.: Nanotechnol. Biol. Med.* **2012**, *8*, 1355−1363.
(80) Quellec, P.; Gref, R.; Perrin, L.; Dellacherie, E.; Sommer, F.; Verbavatz, J. M.; Alonso, M. J. Protein Encapsulation within Polyethylene Glycol-Coated Nanospheres. I. Physicochemical Characterization. *J. Biomed. Mater. Res.* **1998**, *42*, 45−54.
(81) Chen, J.-L.; Yan, X.-P.; Meng, K.; Wang, S.-F. Graphene Oxide Based Photoinduced Charge Transfer Label-Free near-Infrared Fluorescent Biosensor for Dopamine. *Anal. Chem.* **2011**, *83*, 8787−8793.
(82) Tang, C. Y.; Kwon, Y.-N.; Leckie, J. O. Fouling of Reverse Osmosis and Nanofiltration Membranes by Humic Acid-Effects of Solution Composition and Hydrodynamic Conditions. *J. Membr. Sci.* **2007**, *290*, 86−94.
(83) Do, V. T.; Tang, Y. C.; Reinhard, M.; Leckie, J. O. Degradation of Polyamide Nanofiltration and Reverse Osmosis Membranes by Hypochlorite. *Environ. Sci. Technol.* **2012**, *46*, 852−859.

DOI: 10.1021/am509174j
ACS Appl. Mater. Interfaces 2015, 7, 11117−11126